Title

Simultaneous Metabolic and Perfusion Imaging Using Hyperpolarized 13C MRI Can Evaluate Early and Dose-Dependent Response to Radiation Therapy in a Prostate Cancer Mouse Model

Journal

International Journal of Radiation Oncology • Biology • Physics, 107(5)

ISSN

0360-3016

Authors

Qin, Hecong
Zhang, Vickie
Bok, Robert A
et al.

Publication Date

2020-08-01

DOI

10.1016/j.ijrobp.2020.04.022

Peer reviewed

HHS Public Access

Author manuscript

Int J Radiat Oncol Biol Phys. Author manuscript; available in PMC 2021 August 01.

Published in final edited form as:

Int J Radiat Oncol Biol Phys. 2020 August 01; 107(5): 887–896. doi:10.1016/j.ijrobp.2020.04.022.

Simultaneous metabolic and perfusion imaging using hyperpolarized ^{13}C MRI can evaluate early and dose-dependent responses to radiotherapy in a prostate cancer mouse model

Hecong Qin[1,3,*], **Vickie Zhang, PhD**[1], **Robert A. Bok, MD, PhD**[1], **Romelyn Delos Santos, MD**[1], **J. Adam Cunha, PhD**[2], **I-Chow Hsu, MD**[2], **Justin Delos Santos**[1], **Jessie E. Lee, PhD**[1], **Subramaniam Sukumar, PhD**[1], **Peder E. Z. Larson, PhD**[1,3], **Daniel B. Vigneron, PhD**[1,3], **David M. Wilson, MD, PhD**[1,§], **Renuka Sriram, PhD**[1,§], **John Kurhanewicz, PhD**[1,3,§]

[1]Department of Radiology and Biomedical Imaging, University of California, San Francisco

[2]Department of Radiation Oncology, University of California, San Francisco

[3]UC Berkeley - UCSF Graduate Program in Bioengineering, University of California, Berkeley and University of California, San Francisco

Abstract

Purpose: To investigate using a novel imaging approach - hyperpolarized (HP) ^{13}C magnetic resonance imaging (MRI) for simultaneous metabolism and perfusion assessment - to evaluate early and does-dependent radiotherapy (RT) response in a prostate cancer mouse model.

Methods and Materials: Transgenic Adenocarcinoma of Mouse Prostate (TRAMP) mice (n = 18) underwent singlefraction RT (4 - 14 Gy steep dose across the tumor) and were imaged serially at pre-RT baseline and 1, 4, and 7 days post-RT, using HP ^{13}C MRI with combined [1-^{13}C]pyruvate (metabolic active agent) and [^{13}C]urea (perfusion agent), coupled with conventional multiparametric ^{1}H MRI including T_2-weighted, dynamic contrast-enhanced (DCE), and diffusion-weighted imaging. Tumor tissues were collected at Day 4 and Day 7 for biological correlative studies.

Results: We found a significant decrease in HP pyruvate-to-lactate conversion in tumors responding to RT, with concomitant significant increases in HP pyruvate-to-alanine conversion and HP urea signal; whereas the opposite changes were observed in tumors resistant to RT. Moreover, HP lactate change was radiation-dose dependent: tumor regions treated with higher radiation doses (10-14 Gy) exhibited a greater decrease in HP lactate signal than low-dose regions (4-7 Gy) as early as 1 day post-RT, consistent with LDH enzyme activity and expression data. We also found

Corresponding Authors: John Kurhanewicz, Ph.D., Department of Radiology and Biomedical Imaging, University of California, San Francisco, 1700 4th Street, Byers Hall Suite 203, San Francisco, CA 94158-2330. Phone: 415-514-9711; Fax: 415-514-9714; john.kurhanewicz@ucsf.edu.

*Author responsible for statistical analyses: Hecong Qin, Department of Radiology and Biomedical Imaging, University of California, San Francisco, 1700 4th Street, Byers Hall Suite 203, San Francisco, CA 94158-2330.

§co-senior authors

that HP [^{13}C]urea MRI provided similar assessments of tumor perfusion to those provided by ^{1}H DCE MRI in this animal model. However, apparent diffusion coefficient (ADC), a conventional ^{1}H MR functional biomarker, did not exhibit statistically significant changes within 7 days after RT.

Conclusion: These results demonstrate the ability of HP ^{13}C MRI to monitor radiation-induced physiologic changes in a timely and dose-dependent manner, providing the basic science premise for further clinical investigations and translation.

Summary

Hyperpolarized ^{13}C MRI detected early and dose-dependent radiotherapy response in a transgenic prostate cancer mouse model as early as 1 day post-therapy. This novel molecular imaging technique can provide simultaneous assessment of tumor metabolism and perfusion and be combined with the existing state-of-the-art multiparametric MRI, marking its clinical translation potential for improved radiotherapy assessment.

I. Introduction

Radiotherapy (RT), including external beam RT and brachytherapy, is the standard management option for both localized and advanced prostate cancer (PCa) (1, 2). Despite the technical advances in RT, treatment failure and disease recurrence are common and place a significant burden on PCa patient care (3, 4). Specifically, treatment failure at the targeted tumor site is the primary mode of PCa recurrence post-RT, suggesting inadequate targeting, dose delivery, and intrinsic radioresistance (5–7). Although a lower prostate-specific antigen (PSA) nadir is associated with improved outcomes, absolute PSA levels are inadequate to distinguish treatment failure from treatment success. In addition, post-RT PSA decreases are slow, taking an average of 18 months before reaching the nadir, therefore, unable to provide early or tumor-specific evaluations (8). These clinical challenges have motivated the development of imaging technologies that can detect early and localized RT response or failure.

Imaging has played an expanding role in RT planning and evaluation. Increasingly, molecular and functional imaging tools, including positron emission tomography (PET) and ^{1}H multiparametric MRI, have been applied to guide RT planning, evaluate post-RT responses, and identify cancer recurrence (9–12). Hyperpolarized (HP) ^{13}C MRI is a paradigm-shifting molecular imaging technology for cancer diagnosis and therapy monitoring with a unique ability to study real-time metabolism and perfusion simultaneously. HP ^{13}C MRI is enabled by dissolution dynamic nuclear polarization (dDNP), which provides over 5 orders of magnitude signal enhancement for ^{13}C enriched, non-radioactive imaging agents (13, 14). HP [1-^{13}C]pyruvate MRI has allowed direct visualization of glycolysis in PCa patients (15), and numerous clinical studies are ongoing to characterize cancer aggressiveness and response to targeted therapies (16, 17). HP [1-^{13}C]pyruvate can be co-polarized and imaged with HP [^{13}C]urea to assess metabolism and perfusion simultaneously, providing new measures of cancer aggressiveness and therapy response (18–21).

Radiation induces cell cycle arrest, senescence, apoptosis, and eventual cell death (22, 23), resulting in decreased glycolytic flux; therefore, a decrease in HP ^{13}C pyruvate-to-lactate conversion rate may reflect metabolic remission following RT. In contrast, high tumor lactate content post-RT and the associated lactate dehydrogenase (LDH) overexpression have been shown to be associated with a radioresistant phenotype (24–26). These differential metabolic profiles between radiosensitive and radioresistant tumors provide a strong rationale to study lactate metabolism for RT assessment. Additionally, the pyruvate-to-lactate conversion rate also depends on the concentration of nicotinamide adenine dinucleotide (NADH), a cofactor in LDH reduction of pyruvate. Since NADH modulates the cellular reducing potential, the rate of HP ^{13}C pyruvate-to-lactate reduction may also reflect oxidative stress induced by ionizing radiation (27). RT also causes complex changes to tissue perfusion and cellularity (28, 29). As a metabolically inert agent without background signals, HP [^{13}C]urea MRI can trace the vascular delivery and interstitial distribution, thereby assessing tissue perfusion similar to the gadolinium-based contrast agent (GBCA) for dynamic contrast-enhanced (DCE) MR. Thus, HP [1-^{13}C]pyruvate and [^{13}C]urea are ideal imaging probes to study the biological processes implicated in RT resistance and response.

In this study, we applied HP MRI using combined [1-^{13}C]pyruvate and [^{13}C]urea to examine early and dose-dependent tumor responses to RT. We also incorporated DCE MR and diffusion-weighted imaging (DWI), two clinical standard techniques in multiparametric ^{1}H MRI, to assess changes to the tumor microenvironment, and to investigate their concordance with HP data. We hypothesized that 1) dual-probe HP ^{13}C and multiparametric ^{1}H MRI could detect altered tumor physiology within days following RT, and 2) these changes are associated with both therapeutic response and radiation dose.

II. Methods

Study Design:

All animal procedures were approved by our Institutional Animal Care and Use Committee (IACUC). Transgenic Adenocarcinoma of Mouse Prostate (TRAMP, C57BL/6xFVB, Roswell Park Cancer Institute, Buffalo, NY) mice (n = 18) underwent singlefraction RT and were imaged serially using HP ^{13}C MRI and multiparametric MRI including T_2-weighted imaging, DCE MRI, and DWI. Imaging study time points included pre-therapy and 1,4, and 7 days post-therapy, and mice were sacrificed for tissue collection at Day 4 (n = 4) and Day 7 (n = 7). RT was delivered by a microSelectron® brachytherapy system (Elekta/Nucletron, Veenendaal, the Netherlands) with a high-dose rate applicator and Ir-192 as the radiation source. A 10 Gy radiation dose in a single fraction was prescribed to a 3 mm depth, providing a steep dose gradient across the tumor ranging from 4 to 14 Gy. Treatment-planning CT images (Siemens, Malvern, PA) and radiation dose distribution maps (Oncentra® Brachy software, Elekta/Nucletron) were obtained to investigate dose-dependent tumor response.

Imaging methods:

All MRI experiments were performed on a 14.1 Tesla Varian MR microimaging system (Agilent Technologies, Santa Clara, CA). Dynamic nuclear polarization was performed on a HyperSense™ polarizer (Oxford Instruments, Abingdon, UK): [1-^{13}C]pyruvic acid and [^{13}C]urea were co-polarized and subsequently injected intravenously, as previously described (30). Metabolite-specific imaging was performed using a single-shot, threedimensional (3D) Gradient And Spin Echo (GRASE) sequence to image HP [1-^{13}C]lactate, [1-^{13}C]alanine, [1-^{13}C]pyruvate, [^{13}C]urea, and HP001 (a frequency-calibration phantom) sequentially, as previously described (20, 21). Detailed imaging methods, including multiparametric MRIs, are reported in the Supplementary Material.

Image analysis:

Tumor volumes were measured on T_2-weighted MR images using in-house developed software (BRIMAGE). All other image analyses were performed on a pixel-by-pixel basis using MATLAB 2018b (Mathworks, Natick, MA). Normalized [1-^{13}C]lactate signal (nLac) was calculated as the percentage of lactate to pyruvate and its downstream metabolites, "lactate/(pyruvate + lactate + alanine)," and [^{13}C]urea signal was normalized to the sum of [^{13}C]urea signal within the imaging volume (lower abdomen and pelvis of the mouse) to account for variations in polarization levels and transfer time. Signal-to-noise ratio (SNR) was calculated using Rician noise for magnitude images, and only voxels with SNR greater than 3 were included (31, 32). HP [1-^{13}C]alanine has considerably lower signal than other metabolites, and is quantified as a percentage of tumor voxels with SNR greater than 3.

Semi-quantitative DCE parameters were computed based on GBCA concentration (mM), including initial area under the curve (iAUC) (sum of 90 seconds from the start of injection), wash-in slope (mM/min), and wash-out slope (mM/min). Detailed DCE image analysis methods are reported in the Supplemental Materials. For DWI analysis, apparent diffusion coefficients (ADC, x 10^{-3} mm^2/s) were estimated based on linear fitting of diffusion-weighted signal of 4 b-values to the equation $S = S_0 \cdot exp(-\mathrm{ADC} \cdot \mathrm{b})$ using VNMRJ software (Agilent Technologies, Santa Clara, CA).

Radiation dose maps were co-registered with MRI images using a rigid registration algorithm based on Mattes Mutual information registration metric using an open-source software 3D Slicer (33). To mitigate the registration error, we grouped the radiation dose ranges into only 3 categories (Figure 3A: high: 10-14 Gy; intermediate: 7-10 Gy; low: 4-7 Gy), rather than performing a linear dose-response correlation. A subset of mice (n = 7) did not have congruent radiation dose maps. Tumor regions of interest (ROIs) were manually drawn on the T_2-weighted, DWI, and DCE images, and then applied to ^{13}C images. The means of imaging parameters of the whole tumor as well as tumor regions treated with low (4-7 Gy), intermediate (7-10 Gy), and high (10-14 Gy) radiation doses were calculated.

Biological correlations:

TRAMP tumors were harvested at four (n = 4) or seven days (n = 7) post-RT: Tumor tissues corresponding to high and low radiation doses were excised after reviewing the corresponding T_2-weighted MR images and registered dose maps prior to dissection; the

intermediate zones were avoided, only comparing the tumor cross-sectional specimens of high dose (ventral) vs low dose (dorsal) regions, which were spatially well separated due to the directionality of the radiation dose gradient. In addition, one group of untreated TRAMP tumors (n = 11) of similar tumor stage were harvested as the untreated control. Immunohistochemistry (IHC), including anti-Ki-67 and anti-caspase-3/ASP175 staining; gene expression assays for relevant transporters and enzymes in glycolic metabolism, including lactate dehydrogenase-α, -β (LDH-A,B), and monocarboxylate transporters 1 and 3/4 (MCT1, 3/4); and LDH enzyme activity assay were performed. Quantifications of IHC staining were obtained by visual microscopic inspection to assess percentage of positively stained cells, employing iterative inspections at various magnification levels over an entire tumor crosssection. Detailed methods are reported in the Supplementary Material.

Statistical analysis:

Changes in imaging parameters of the whole tumor were evaluated using multilevel regression analyses (reported in the Supplementary Material and Table S1). The relationship between imaging parameters and radiation doses was evaluated by a repeated measures one-way ANOVA test for each time point, followed by multiple comparisons with Tukey's methods. An ordinary regression analysis with clustered variance structure was used to examine the correlation between non-independent parameters. A paired Student's t-test was used to compare biological parameters from regions treated with high and low radiation doses, and an unpaired t-test was used to compare treated versus untreated control tumors. Data are reported as mean ± standard deviation for descriptive statistics or estimate ± standard error for regression analysis. P values less than .05 are considered statistically significant. All statistical analyses were performed using Stata 16 (StataCorp LLC, College Station, TX) and Prism 8 (GraphPad, San Diego, CA).

III. Results

Changes in tumor metabolism and perfusion by hyperpolarized ^{13}C MRI are indicative of post-radiotherapy response.

Modeled after the revised RECIST criteria (34), mice with increased tumor volumes, as measured on T_2-weighted images, 4 days after RT were considered non-responders, and otherwise considered responders. Out of 18 RT-treated mice, 14 are responders with the following tumor volume changes: 70.3 ± 16.7% of baseline at Day 4 ($P < .0001$), 73.4 ± 11.1% at Day 7 ($P = .0002$); 4 are non-responders :115.5 ± 7.1% at Day 4 ($P = .090$), 140.3 ± 7.1% at Day 7 ($P = .0008$) (Figure S1). Responders and non-responders have similar baseline tumor volumes (2.61 ± 1.82 vs. 2.81 ± 1.95 cc, $P = .85$). Figure 1 shows a representative serial imaging study using HP ^{13}C and multi-parametric ^{1}H MRI in a mouse responding to RT.

Pyruvate-to-lactate conversion is the major energy-producing metabolic flux in aerobic glycolysis and is NADH-dependent. For responders, normalized HP [1-^{13}C]lactate (nLac) did not change substantially at Day 1 ($P = .97$, n = 16), but decreased significantly at Day 4 by .05 ± .02 ($P = .023$, n = 15) and by .11 ± .02 at Day 7 ($P < .0001$, n = 11) (Figure 2A). In contrast, no significant changes were observed in non-responders. A multilevel regression

analysis showed that nLac decreased significantly for responders ($P < .0001$), but slightly increased for nonresponders ($P = .32$), and their rates of change were significantly different ($P = .021$) (Figure S2A).

We also evaluated the pyruvate-to-alanine flux, an alternative and competing metabolic flux to pyruvate-to-lactate conversion: In contrast to post-RT [1-^{13}C]lactate changes, [1-^{13}C]alanine (% of voxels with detectable alanine) (Figure 2B) increased by 4.29 ± 3.64% at Day 1 ($P = .25$), by 10.96 ± 3.76% at Day 4 ($P = .006$), and by 11.68 ± 4.21% at Day 7 ($P = .0086$), with no significant changes for non-responders. A multilevel regression analysis revealed that HP alanine increased significantly after RT in responders ($P = .0017$), and slightly decreased in non-responders ($P = .32$), with significantly different rates of change ($P = .013$) (Figure S2B).

HP [^{13}C]urea was co-injected with HP [1-^{13}C]pyruvate as an extracellular perfusion agent. For the responders, normalized HP [^{13}C]urea signal (arbitrary units) slightly increased by 4.22 ± 7.13% at Day 1 relative to baseline ($P = .56$), but increased significantly by 24.81 ± 7.34% at Day 4 ($P = .0017$) and by 38.34 ± 8.24% at Day 7 ($P < .0001$) (Figure 2C). A multilevel regression analysis (Figure S2C) revealed that the normalized [^{13}C]urea signal increased significantly in responders ($P < .0001$), but decreased significantly in non-responders ($P = .0037$), with significantly different rates of change ($P < 0.0001$). Finally, at pre-RT baseline, there were no significant differences between responders and non-responders in HP lactate, HP alanine, or HP urea ($P = .14, .83, .085$, respectively).

DCE and DWI ^{1}H MRI corroborate HP ^{13}C MRI assessments of tumor physiology and microenvironment following radiotherapy.

^{1}H DCE MRI and DWI were used to further evaluate tumor physiology and microenvironment changes following RT as a companion to HP ^{13}C MRI. For responders (n = 12), GBCA accumulation (iAUC, mM, Figure S3A) significantly increased ($P = .0003$), wash-in slope (mM/min, Figure S3B) significantly increased ($P = .0002$), with significantly enhanced wash-out slope (became more negative) (mM/min, Figure S3C) ($P = .0075$), indicative of increased contrast delivery and clearance following RT. The nonresponders (n = 4) showed the opposite changes: iAUC slightly decreased ($P = .39$) and wash- in slope slightly decreased ($P = .50$), with significantly different rates of change from responders ($P = .0072, .0099$, respectively). The changes in wash-out slopes were not significantly different between responders and non-responders ($P = .32$). There were no significant differences at baseline between responders and non-responders in iAUC, wash-in slopes, or wash-out slopes ($P = .25, .22, .90$, respectively). Finally, HP [^{13}C]urea signal significantly correlated with iAUC ($P = .049$) despite their considerably different imaging contrast mechanisms, quantification methods, and numerical scales (Figure S3D).

As a functional imaging technique, DWI generates apparent diffusion coefficient (ADC) maps that assess tissue cellularity. We found ADC ($\times 10^{-3}$ mm^2/s) slightly decreased in responders ($P = 0.17$, n = 14) and slightly increased in non-responders ($P = .15$, n = 4); the differences in ADC changes were close to statistical significance ($P = 0.057$) (Figure S4). Moreover, non-responder tumors had significantly lower ADCs at pre-therapy baseline compared to responders (by $0.31 \pm 0.13 \times 10^{-3}$ mm^2/s, $P = .025$).

Intratumoral changes in hyperpolarized ^{13}C pyruvate-to-lactate conversion are radiation dose-dependent.

Through radiation dose mapping, each tumor was divided into high- (10-14 Gy), intermediate- (7-10 Gy), and low-dose (4-7 Gy) regions. Since we sought to investigate the localized dose-dependent tumor response to RT, responders or non-responders were not distinguished for dose-analysis. We found that the magnitude of nLac changes from baseline was significantly associated with radiation dose (ANOVA: Day 1, $P = .045$, n = 11; Day 4, $P = 0.040$, n = 10; Day 7, $P = .0003$, n = 9). High-dose regions showed significantly greater nLac decrease than low-dose regions as early as Day 1, and the effect size also increased over time (Figure 4: Day 1, $P = .038$, Cohen's d = .71; Day 4, $P = .042$, d = .75; Day 7, $P = .0022$, d = 1.22; adjusted for multiple comparisons). Furthermore, the decrease in nLac in the high-dose region at Day 1 ($P = .07$) is an early indication of tumor response to RT, with subsequent significant decreases on Day 4 and Day 7 ($P = .038$, $P = .0003$, respectively). Intermediate-dose regions also showed a slight decrease at Day 4 ($P = .092$) and a significant decrease at Day 7 ($P = .0001$), but there were no significant changes in the low-dose regions. Since the intratumoral heterogeneity at pre-therapy baseline is a confounding factor, we compared multiple baseline MRI parameters among three dose regions and found no significant difference in baseline intratumoral nLac ($P = .10$). Comparisons of other baseline MRI parameters were reported in Figure S5.

Ex vivo correlative studies showed dose-dependent decreases in markers of tumor proliferation and glycolysis following radiotherapy.

In tumor regions treated with high-dose radiation, the histological sections showed hypo-cellularity with necrosis and fibrosis (Figure 4A, H&E), nuclear shrinkage, and vacuolation; low-dose regions showed similar changes but to a lesser degree. In contrast, the untreated control tumor exhibited high cellularity, nuclear atypia, and no vacuolation on histology. Quantitively, high-dose regions showed significantly higher necrosis and fibrosis than low-dose regions and untreated controls (Figure 4B; $P = .0024$, $P = .029$, respectively), and significantly lower anti-Ki-67 staining (Figure 4C; $P = .0002$, $P = .0018$ respectively). High-dose regions also had non-significant higher anti-Caspase-3 staining (an apoptosis marker) than untreated tumors (Figure 4D).

The high-dose regions also showed decreased LDH enzyme activity than low-dose regions and untreated tumors (Vmax, mM NADH/min/[protein]; $P = .042$, $P = .0001$, respectively), as well as LDHA expression (relative expression fold; $P = .022$, $P < .0001$, respectively), as shown in Figure 4E, F. Similarly, the low-dose region also showed lower LDH activity and LDHA expression than untreated tumors ($P = .0067$, $P = .0014$, respectively). Moreover, there was a weak correlation between LDH activity and changes in HP ^{13}C lactate signal on a per subject basis ($P = .16$). We also found the expression of LDHB, the competing isoform to LDHA, was slightly higher in the high-dose regions that low-dose regions, although the difference was not statistically significant (Figure 4G). Additionally, there was no significant difference in MCT1 (the transporter responsible for pyruvate import) among three groups (Figure 4G), but high-dose regions exhibited significantly lower expression of MCT 3/4 (the transporter responsible for lactate export) than low-dose regions and untreated tumors ($P = .16$, $P = .0054$, respectively) (Figure 4H).

IV. Discussion

Although enormous progress has been made in RT precision and efficacy, many patients still suffer from post-radiation cancer recurrence. Non-invasive, sensitive imaging markers of tumor response to RT are needed to personalize patient care. In this study, we used HP ^{13}C and multiparametric ^{1}H MRI to characterize early and dose-dependent tumor responses to RT, accomplished by co-administration of HP [1-^{13}C]pyruvate and HP [^{13}C]urea in TRAMP mice that were also imaged with DCE MRI and DWI. We found that in TRAMP tumors responding to RT, HP [1-^{13}C]lactate production decreased significantly, with a concomitant increase in alanine production and tumor perfusion as measured by both HP ^{13}C urea and DCE MRI. In contrast, the opposite changes were observed in tumors that did not respond to RT. The post-radiation MRI changes are consistent with the tumor pathophysiology and their responses to radiation. Glycolytic metabolism and perfusion are both interrelated and central to tumor biology (25). Radiation-induced DNA damages cause cell cycle arrest or death, effectively halting tumor proliferation and metabolic demands. The decreased HP ^{13}C pyruvate-to-lactate conversion is consistent with the decreased LDHA expression and LDH enzyme activity. Moreover, radiation-induced reactive oxygen species (ROS) deplete NADH (35), the cofactor required for pyruvate-to-lactate conversion, contributing to the decreased lactate production. The transamination of pyruvate to alanine is an alternative and competing enzymatic flux to the reduction of pyruvate to lactate, and we found that HP lactate and alanine changed in the opposite directions after RT, consistent with the observation when NAD biosynthesis was inhibited in a prior study (36). Radiation-induced inflammation is a confounding factor for interpretation of HP lactate: The activation and infiltration of immune cells could *elevate* the HP ^{13}C lactate signal in tumor tissue responding to RT. However, the significantly *decreased* post-RT lactate suggests that metabolic remission is the predominate biological process responsible for the HP ^{13}C lactate change. Finally, the increased tumor perfusion seen by HP [^{13}C]Urea MRI and DCE may be related to increased permeability from radiation-induced vascular damage and inflammation. Overall, the synergy between metabolic and perfusion imaging is evident in this study, providing sharp contrasts and sensitive metrics for therapy evaluation. Together, these results suggest that decreased lactate production, increased alanine production, and increased perfusion are acute tumor responses to effective radiotherapy. Conversely, increased lactate production with decreased alanine production and perfusion are indicative of aggressive and radioresistant phenotypes.

With a radiation dose mapping technique, we found a continuum of radiation dose-dependent effect in HP ^{13}C lactate decreases (high-dose regions exhibit greater changes than intermediate-dose regions, which show greater changes than low-dose regions), consistent with dose-dependent changes in the cell proliferation, LDH expression and activity. Moreover, this localized dose dependency was evident as early as Day 1 and became more pronounced at Day 4 and Day 7. The very large effect size (more than 1.2) of HP [1-^{13}C]lactate decrease at Day 7 after RT, an optimal intervention window, makes HP [1-^{13}C]lactate a desirable imaging marker for further clinical investigation. With the wide use of dose escalation techniques, a dose-dependent functional imaging metrics could be an invaluable tool for RT planning and evaluation. However, few imaging studies have explored the radiation dose-dependent effects (37, 38). Our study, for the first time, demonstrated the

radiation dose-dependent effects in a tumor model using non-invasive *in vivo* imaging techniques.

The HP ^{13}C MRI findings should be interpreted in the context of other preclinical studies. Matsuo et al. (39) found that 5 Gy irradiation caused increased tumor HP lactate production and decreased perfusion 24 hours after RT. Additionally, Sandulache et al. (27) showed that 5 Gy irradiation caused a transient decrease (about 30 minutes) in HP lactate signal in cancer cells. The treatment regimens used in these two studies correspond to the low-dose tumor regions in our study. In a few low-dose tumor regions, we observed slightly increased lactate production on Day 1 and Day 4 (Figure 3); however, for the whole cohort, no significant changes in the low-dose regions were observed. These data suggest that higher radiation doses are required to render metabolic changes detectable by HP [1-^{13}C]pyruvate MRI. Indeed, Day et al. (40) showed when rats bearing glioma tumors were treated with 15 Gy radiation, HP ^{13}C lactate signal diminished significantly three days following RT, with associated prolonged survival. Additionally, Chen et al. (41) observed a decreased HP ^{13}C lactate-to-pyruvate ratio 4 days post 8 Gy irradiation but found no significant changes in perfusion.

In this study, we adopted multiparametric ^{1}H MRI, namely DCE MRI and DWI, as companion imaging markers, and compared HP ^{13}C MRI against clinical standard techniques for RT assessments. DCE MRI demonstrated the same contrastive perfusion changes between responders and non-responders, and there was a correlation between DCE iAUC and HP ^{13}C urea MRI on a per subject basis, validating the efficacy of HP ^{13}C urea MRI as a perfusion imaging technique. The main advantage of HP [^{13}C]urea is that it can be combined with other HP ^{13}C probes in a single imaging session, providing simultaneous probe delivery and tissue perfusion assessment. Moreover, compared to Gd-based DCE MRI, [^{13}C]urea is an endogenous compound with almost no toxicity.

RT renders complex tissue microenvironment changes such as cellular edema in the short term (lowering ADC) and decreased cellularity long term (increasing ADC). Thus, this opposing change complicates the interpretation of ADC in the context of RT assessment. Although we found non-responders had significantly lower baseline ADC than responders, there were no significant changes in ADC post-RT; in fact, ADC slightly decreased for responders and increased for non-responders. Previous literature has reported that a *lower* post-RT ADC indicates favorable outcomes in glioma patients (29, 42), while an *increased* post-RT ADC is a favorable prognostic factor in hepatocellular carcinoma patients(43). This study suggests that HP ^{13}C MRI could provide information that is potentially unavailable from conventional ^{1}H multiparametric MRI.

Our study has several limitations. First, animal models do not fully recapitulate human tumor biology. Hypoxia is a common feature of rodent tumors, especially for large-sized tumors (44). Ventral sides of tumors (high-dose regions) may suffer more from diffusion-limited hypoxia and are therefore more radioresistant; indeed, we found at baseline high-dose tumor regions had a slightly lower lactate metabolism, significantly lower urea perfusion, significantly slower DCE wash-out slopes, and significantly higher cellularity compared to lower dose regions (dorsal side) (Figure S5). Despite the potential

radioresistant phenotypes, we observed a greater magnitude of lactate decrease in the high-dose regions, suggesting HP ^{13}C lactate is a sensitive marker for RT response. Moreover, given the high cellularity of TRAMP tumors, perfusion imaging metrics are heavily weighted by extracellular space and interstitial volume (19), in contrast to human tumors in which enhanced vascularization is the underlying pathophysiology. Another limitation of the study is that DCE, DWI, dose mapping, or tissue collection were not performed for all subjects due to technical and logistical constraints. But since each analysis was relatively independent of each other, the unbalanced sample size should not significantly impact the main findings. Moreover, statistical significances should be interpreted with caution given the relatively small sample sizes; additional studies are needed to validate the observations, especially in clinical settings. Finally, we employed multiple follow-up studies to characterize the post-RT changes, which are not clinically feasible. In future clinical studies, simple pre- and post-RT comparisons should be performed.

Overall, we demonstrated that simultaneous metabolic and perfusion imaging with HP ^{13}C MRI could assess early and dose-dependent tumor response to radiotherapy in a PCa mouse model. This report highlights the clinical translation potential of HP ^{13}C MRI, which is currently being investigated at multiple sites as a cancer diagnosis and therapy monitoring tool. The findings of this study provided the basic science premise for further clinical investigation. With tumor-specific functional evaluations provided by metabolic and perfusion imaging, radiation oncologists could potentially personalize treatment regimens, verify radiation dose delivery, and discern treatment response or failure.

Supplementary Material

Refer to Web version on PubMed Central for supplementary material.

Acknowledgments

The authors acknowledge the Biomedical NMR Lab, the Surbeck Lab of Advanced Imaging, and Hyperpolarized MRI Technology and Resource Center (HMTRC) at the University of California, San Francisco for technical and administrative supports; and Dr. Barbara Foster at Roswell Park Cancer Institute for supplying Transgenic Adenocarcinoma of Mouse Prostate (TRAMP) mice used in this study. HQ acknowledges Genentech Foundation Predoctoral Fellowship.

Funding information

This work was supported by research grants from National Institute of Health (NIH): R01CA214554 (JK), R01CA166655(JK), P41EB013598(DV, JK), and R01CA166766 (DW).

Conflicts of Interest Statement

JK, DV, PL report grants from GE Healthcare during the conduct of the study and outside the submitted work. PL also reports personal fees from Human Longevity Inc, outside the submitted work. Other authors declare no conflicts of interest.

Reference

1. Sanda MG, Cadeddu JA, Kirkby E, et al. Clinically localized prostate cancer: AUA/ASTRO/SUO guideline. part I: risk stratification, shared decision making, and care options. J. Urol. 2018;199:683–690. [PubMed: 29203269]

2. Chin J, Rumble RB, Kollmeier M, et al. Brachytherapy for patients with prostate cancer: american society of clinical oncology/cancer care ontario joint guideline update. J. Clin. Oncol. 2017;35: 1737–1743. [PubMed: 28346805]

3. Roach M, Hanks G, Thames H, et al. Defining biochemical failure following radiotherapy with or without hormonal therapy in men with clinically localized prostate cancer: recommendations of the RTOG-ASTRO Phoenix Consensus Conference. Int. J. Radiat. Oncol. Biol. Phys. 2006;65:965–974. [PubMed: 16798415]

4. Cox JD, Gallagher MJ, Hammond EH, et al. Consensus statements on radiation therapy of prostate cancer: guidelines for prostate re-biopsy after radiation and for radiation therapy with rising prostate-specific antigen levels after radical prostatectomy. American Society for Therapeutic Radiology and Oncology Consensus Panel. J. Clin. Oncol. 1999; 17:1155. [PubMed: 10561174]

5. Jalloh M, Leapman MS, Cowan JE, et al. Patterns of Local Failure following Radiation Therapy for Prostate Cancer. J. Urol. 2015;194:977–982. [PubMed: 25983194]

6. Hayman J, Hole KH, Seierstad T, et al. Local failure is a dominant mode of recurrence in locally advanced and clinical node positive prostate cancer patients treated with combined pelvic IMRT and androgen deprivation therapy. Urol Oncol. 2019;37:289.e19–289.e26.

7. Arrayeh E, Westphalen AC, Kurhanewicz J, et al. Does local recurrence of prostate cancer after radiation therapy occur at the site of primary tumor? Results of a longitudinal MRI and MRSI study. Int. J. Radiat. Oncol. Biol. Phys. 2012;82:e787–93. [PubMed: 22331003]

8. Crook JM, Choan E, Perry GA, et al. Serum prostate-specific antigen profile following radiotherapy for prostate cancer: implications for patterns of failure and definition of cure. Urology. 1998;51:566–572. [PubMed: 9586608]

9. Vogel WV, Lam MGEH, Pameijer FA, et al. Functional imaging in radiotherapy in the netherlands: availability and impact on clinical practice. Clin. Oncol. (R. Coll. Radiol). 2016;28:e206–e215. [PubMed: 27692741]

10. Pereira GC, Traughber M, Muzic RF. The role of imaging in radiation therapy planning: past, present, and future. BiomedRes. Int 2014;2014:231090.

11. Thorwarth D Functional imaging for radiotherapy treatment planning: current status and future directions-a review. Br. J. Radiol. 2015;88:20150056. [PubMed: 25827209]

12. Zhang VY, Westphalen A, Delos Santos L, et al. The role of metabolic imaging in radiation therapy of prostate cancer. NMR Biomed. 2014;27:100–111. [PubMed: 23940096]

13. Ardenkjaer-Larsen JH, Fridlund B, Gram A, et al. Increase in signal-to-noise ratio of > 10,000 times in liquid-state NMR. Proc. Natl. Acad. Sci. USA. 2003;100:10158–10163. [PubMed: 12930897]

14. Hurd RE, Yen Y-F, Chen A, et al. Hyperpolarized 13C metabolic imaging using dissolution dynamic nuclear polarization. J. Magn. Reson. Imaging. 2012;36:1314–1328. [PubMed: 23165733]

15. Nelson SJ, Kurhanewicz J, Vigneron DB, et al. Metabolic imaging of patients with prostate cancer using hyperpolarized [1–13C]pyruvate. Sci. Transl. Med 2013;5:198ra108.

16. Kurhanewicz J, Vigneron DB, Ardenkjaer-Larsen JH, et al. Hyperpolarized 13C MRI: path to clinical translation in oncology. Neoplasia. 2019;21:1–16. [PubMed: 30472500]

17. Wang ZJ, Ohliger MA, Larson PEZ, et al. Hyperpolarized 13C MRI: state of the art and future directions. Radiology. 2019;291:273–284. [PubMed: 30835184]

18. von Morze C, Larson PEZ, Hu S, et al. Investigating tumor perfusion and metabolism using multiple hyperpolarized (13)C compounds: HP001, pyruvate and urea. Magn. Reson. Imaging. 2012;30:305–311. [PubMed: 22169407]

19. Chen H-Y, Larson PEZ, Bok RA, et al. Assessing Prostate Cancer Aggressiveness with Hyperpolarized Dual-Agent 3D Dynamic Imaging of Metabolism and Perfusion. Cancer Res. 2017;77:3207–3216. [PubMed: 28428273]

20. Lee JE, Diederich CJ, Bok R, et al. Assessing high-intensity focused ultrasound treatment of prostate cancer with hyperpolarized 13 C dual-agent imaging of metabolism and perfusion. NMR Biomed. 2018:e3962. [PubMed: 30022550]

21. Bok R, Lee J, Sriram R, et al. The Role of Lactate Metabolism in Prostate Cancer Progression and Metastases Revealed by Dual-Agent Hyperpolarized 13C MRSI. Cancers (Basel). 2019;11.

22. Eriksson D, Stigbrand T. Radiation-induced cell death mechanisms. Tumour Biol. 2010;31:363–372. [PubMed: 20490962]
23. Baskar R, Lee KA, Yeo R, et al. Cancer and radiation therapy: current advances and future directions. Int J Med Sci. 2012;9:193–199. [PubMed: 22408567]
24. Quennet V, Yaromina A, Zips D, et al. Tumor lactate content predicts for response to fractionated irradiation of human squamous cell carcinomas in nude mice. Radiother. Oncol. 2006;81:130–135. [PubMed: 16973228]
25. Sattler UGA, Meyer SS, Quennet V, et al. Glycolytic metabolism and tumour response to fractionated irradiation. Radiother. Oncol. 2010;94:102–109. [PubMed: 20036432]
26. Koukourakis MI, Giatromanolaki A, Panteliadou M, et al. Lactate dehydrogenase 5 isoenzyme overexpression defines resistance of prostate cancer to radiotherapy. Br. J. Cancer. 2014;110:2217–2223. [PubMed: 24714743]
27. Sandulache VC, Chen Y, Lee J, et al. Evaluation of hyperpolarized [1-^{13}C]-pyruvate by magnetic resonance to detect ionizing radiation effects in real time. PLoS One. 2014;9:e87031. [PubMed: 24475215]
28. Taunk NK, Oh JH, Shukla-Dave A, et al. Early Post-treatment Assessment of MRI Perfusion Biomarkers Can Predict Long-term Response of Lung Cancer Brain Metastases to Stereotactic Radiosurgery. Neuro. Oncol. 2017;20:567–575.
29. Hein PA, Eskey CJ, Dunn JF, et al. Diffusion-weighted imaging in the follow-up of treated high-grade gliomas: tumor recurrence versus radiation injury. AJNR Am. J. Neuroradiol. 2004;25:201–209. [PubMed: 14970018]
30. Wilson DM, Keshari KR, Larson PEZ, et al. Multi-compound polarization by DNP allows simultaneous assessment of multiple enzymatic activities in vivo. J. Magn. Reson. 2010;205:141–147. [PubMed: 20478721]
31. Henkelman RM. Measurement of signal intensities in the presence of noise in MR images. Med. Phys 1985;12:232–233. [PubMed: 4000083]
32. Gudbjartsson H, Patz S. The Rician distribution of noisy MRI data. Magn. Reson. Med. 1995;34:910–914. [PubMed: 8598820]
33. Fedorov A, Beichel R, Kalpathy-Cramer J, et al. 3D Slicer as an image computing platform for the Quantitative Imaging Network. Magn. Reson. Imaging. 2012;30:1323–1341. [PubMed: 22770690]
34. Eisenhauer EA, Therasse P, Bogaerts J, et al. New response evaluation criteria in solid tumours: revised RECIST guideline (version 1.1). Eur. J. Cancer. 2009;45:228–247. [PubMed: 19097774]
35. Alhallak K, Jenkins SV, Lee DE, et al. Optical imaging of radiation-induced metabolic changes in radiation-sensitive and resistant cancer cells. J. Biomed. Opt. 2017;22:60502. [PubMed: 28622395]
36. Keshari KR, Wilson DM, Van Criekinge M, et al. Metabolic response of prostate cancer to nicotinamide phophoribosyltransferase inhibition in a hyperpolarized MR/PET compatible bioreactor. Prostate. 2015;75:1601–1609. [PubMed: 26177608]
37. Hahn CA, Zhou S-M, Raynor R, et al. Dose-dependent effects of radiation therapy on cerebral blood flow, metabolism, and neurocognitive dysfunction. Int. J. Radiat. Oncol. Biol. Phys. 2009;73:1082–1087. [PubMed: 18755558]
38. Mahmood U, Alfieri AA, Thaler H, et al. Radiation dose-dependent changes in tumor metabolism measured by 31P nuclear magnetic resonance spectroscopy. Cancer Res. 1994;54:4885–4891. [PubMed: 8069854]
39. Matsuo M, Kawai T, Kishimoto S, et al. Co-imaging of the tumor oxygenation and metabolism using electron paramagnetic resonance imaging and 13-C hyperpolarized magnetic resonance imaging before and after irradiation. Oncotarget. 2018;9:25089–25100. [PubMed: 29861855]
40. Day SE, Kettunen MI, Cherukuri MK, et al. Detecting response of rat C6 glioma tumors to radiotherapy using hyperpolarized [1- 13C]pyruvate and 13C magnetic resonance spectroscopic imaging. Magn. Reson. Med. 2011;65:557–563. [PubMed: 21264939]
41. Chen AP, Chu W, Gu Y-P, et al. Probing early tumor response to radiation therapy using hyperpolarized [1-^{13}C]pyruvate in MDA-MB-231 xenografts. PLoS One. 2013;8:e56551. [PubMed: 23424666]

42. Jakubovic R, Zhou S, Heyn C, et al. The predictive capacity of apparent diffusion coefficient (ADC) in response assessment of brain metastases following radiation. Clin Exp Metastasis. 2016;33:277–284. [PubMed: 26786978]

43. Lo C-H, Huang W-Y, Hsiang C-W, et al. Prognostic Significance of Apparent Diffusion Coefficient in Hepatocellular Carcinoma Patients treated with Stereotactic Ablative Radiotherapy. Sci. Rep 2019;9:14157. [PubMed: 31578433]

44. Moulder JE, Rockwell S. Hypoxic fractions of solid tumors: experimental techniques, methods of analysis, and a survey of existing data. Int. J. Radiat. Oncol. Biol. Phys. 1984;10:695–712. [PubMed: 6735758]

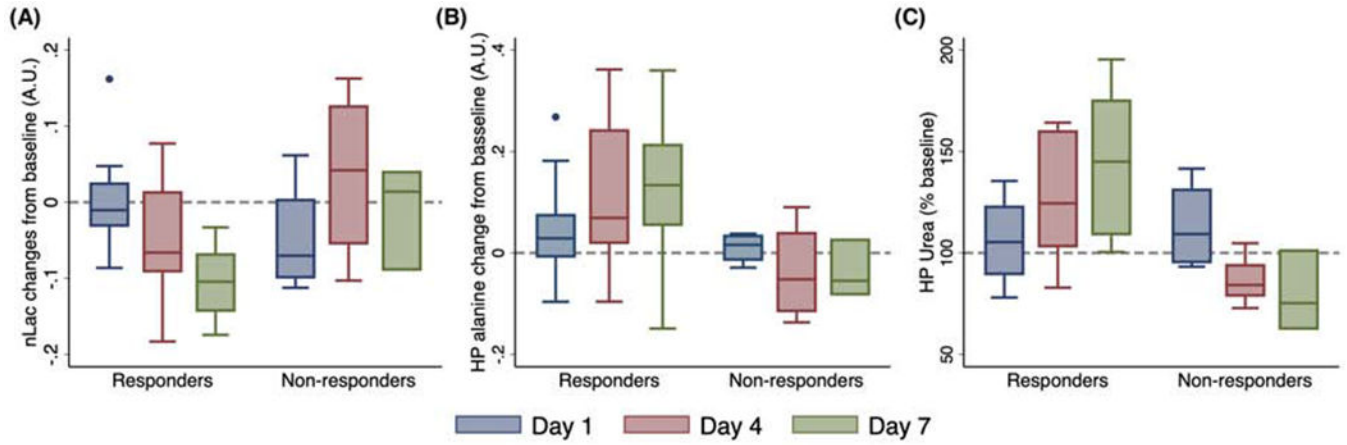

Figure 1:

A panel of representative MR images of a responding mouse prostate tumor following radiotherapy. Tumor volume and hyperpolarized (HP) [1-^{13}C]lactate decreased after radiotherapy, while perfusion increased as shown using HP [^{13}C]urea and dynamic contrast enhanced (DCE) MRI data. There was also an increase in the apparent diffusion coefficient (ADC) in this tumor, which is inversely correlated with cellularity. A frequency-calibration phantom for hyperpolarized ^{13}C scans can be seen in the upper right corner of the images.

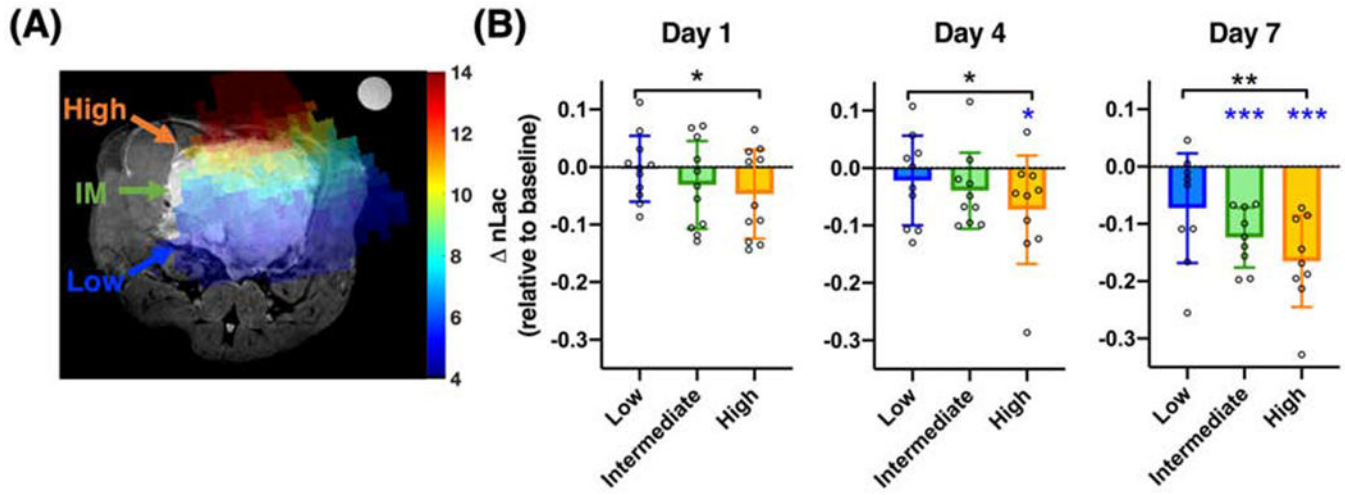

Figure 2:

Changes in normalized hyperpolarized (HP) ^{13}C lactate, alanine, and urea following radiotherapy. There is an apparent decrease in lactate **(A)**, an increase in alanine **(B)** and perfusion as seen in HP [^{13}C]urea **(C)** among volume-decreasing tumors (responders) after radiotherapy. In contrast, there were no apparent changes among non-responders (Day 7 has 3 data points, with overlapping range bars and quantile bars). Multilevel regression analyses revealed a significant decrease in lactate, and significant increases in alanine and urea for responders, and these changes were significantly different from non-responders.

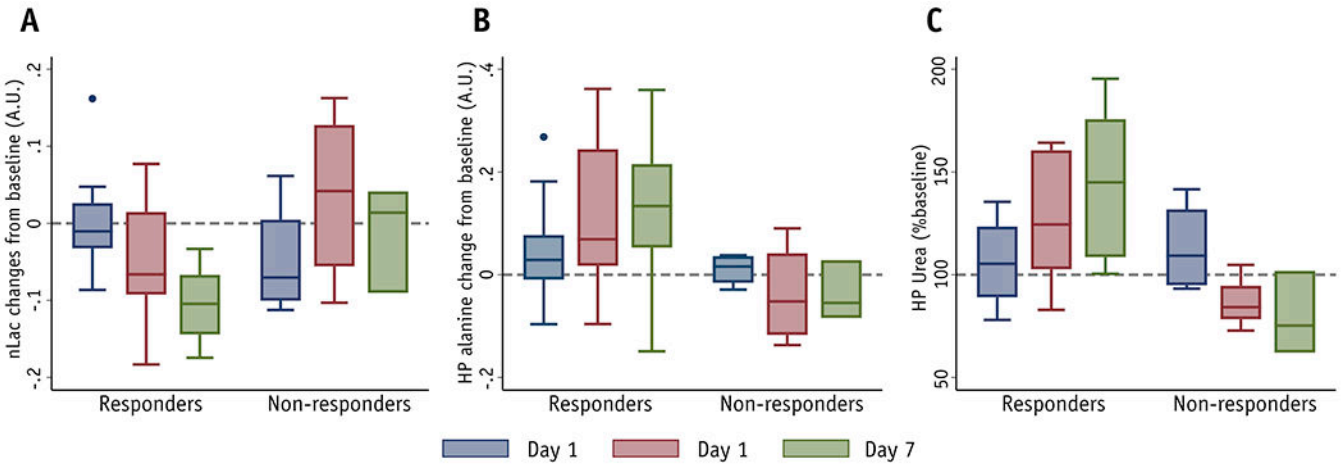

Figure 3:

Intratumoral dose-dependent changes in HP ^{13}C pyruvate-to-lactate conversion. There were significant associations between radiation dose and normalized HP lactate (nLac) changes at all time points. Moreover, high-dose regions (10-14 Gy) showed a greater magnitude of decreases in nLac compared to low-dose regions (4-7 Gy), as early as Day 1. High-dose regions also showed significantly decreased nLac from baseline at Day 4 and Day 7, and intermediate-dose regions also showed significantly decreased nLac from baseline at Day 7 (*, $P < .05$; **, $P < .01$; ***, $P < .001$; black *, ** indicate significant difference between high- and low-dose; blue *, *** indicate significant change from baseline; IM = intermediate).

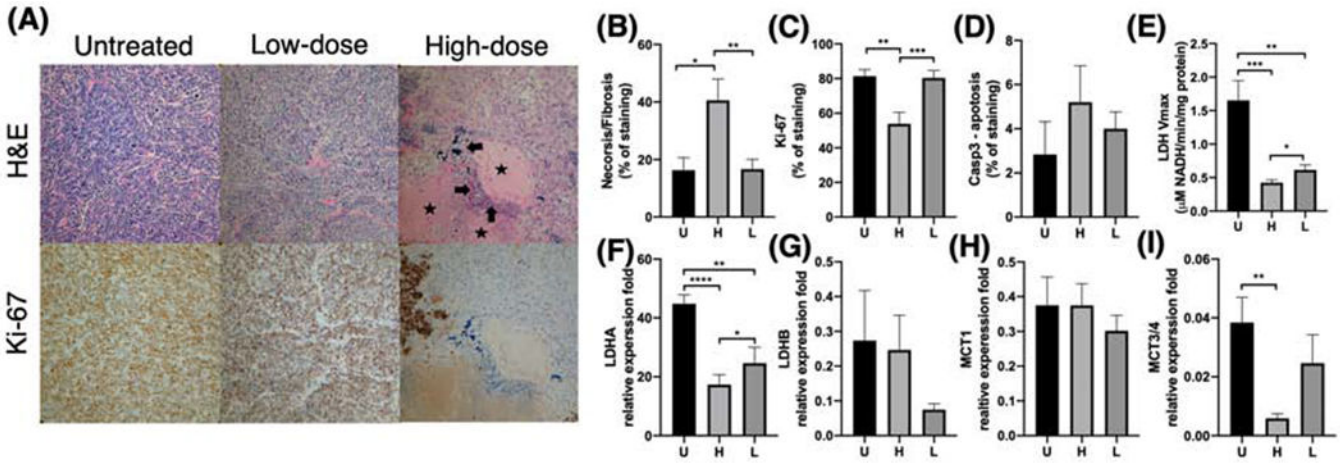

Figure 4:

Dose-dependent changes in immunohistochemical and molecular markers. **Tumor regions treated with high radiation dose** showed significantly more necrosis/fibrosis (**A**: arrows - frank necrosis; stars - frank fibrosis) on H&E staining **(B)** and lower Ki-67 (proliferation) staining **(C)** compared to their corresponding low-dose regions as well as a separate cohort of untreated TRAMP tumors (20x magnification). Moreover, high-dose tumor regions showed lower lactate dehydrogenase (LDH) activity **(E)**, LDHA expression **(F)**, and MCT3/4 expression **(I)** compared to low-dose regions, consistent with the decreased hyperpolarized ^{13}C lactate signal observed in the high dose regions. Additionally, high-dose regions showed slightly higher anti-caspase-3 (an apoptosis marker) staining (**D**), higher LDHB expression (**G**), and lower MCT1 (**H**) expression compared to low-dose regions or untreated tumors, but these differences were not statistically significant. (U = untreated, H = high, L = low; *, $P < .05$; **, $P < .01$; ***, $P < .001$; ****, $p < .001$)